Experimental model-based closed-loop control of a separated boundary layer at high Reynolds number

C. Raibaudo, F. Kerhervé

Experimental model-based closed-loop control of a ~~massively~~ separated boundary layer at high Reynolds number

C. Raibaudo[a,*], F. Kerhervé[a,b]

[a] *École Centrale de Lille, Laboratoire de Mécanique des Fluides de Lille, Cité Scientifique, 59651 Villeneuve d'Ascq Cedex, France*
[b] *Institut PPRIME, CNRS - Université de Poitiers – ISAE-ENSMA - UPR 3346, France*

Abstract

Experimental robust closed-loop control of a two-dimensional turbulent boundary layer with ~~massive~~ *substantial* separation is investigated. An array of 22 round fluidic jets located upstream of the separation location is used as actuation to reattach the flow. Measurements of phase-averaged velocity with 2D2C Particle Image Velocimetry (PIV) and wall friction using hot-film anemometry are performed to characterize the flow dynamics under open-loop actuation to elaborate models of the flow transient. Different feedback model-based controllers (Proportional Intergal, linear-quadratic, linear-quadratic-gaussian and $\mathcal{H}_\infty$ regulators) are then designed and implemented experimentally. The performances in term of precision, reactivity and control cost of each of the controllers are presented and discussed. Only the $\mathcal{H}_\infty$ controller is found to maintain high performances despite large upstream unsteady perturbations.

Keywords: *Separated boundary layer, robust control*

1. Introduction

Separated boundary layers have been, for long, of important interest scientifically and industrially. Flow separation usually occurs due to high adverse pressure gradients (APG) or to abrupt discontinuities in the wall geometry and can lead to important issues in transport applications in terms of drag increase, lift decrease or again sudden loss of the system maneuverability [1]. To prevent separation, flow control has been extensively developed and is now a field of active research. Manipulating a flow with passive actuators thanks to modifications in the geometry or to addition of small objects such as riblets [2] or vortex generators (VG) [3, 4, 5] have proven to be efficient thanks to a redistribution of momentum in the boundary layer [6]. *However, a major drawback of such devices is the lack of adaptability and robustness with regards to sudden changes in the incoming flow due to unsteady perturbations for example.* Modifying the control parameters to alleviate for these sudden changes of the incoming flow is therefore a necessity and one may turn towards active flow control (AFC) solutions.

Active actuators are able to be turned on and off, based on control requirements, and are the main key elements of AFC. By comparison with passive VGs, fluidic active VG jets require fluid supply (air or water) and hence may lead to an increase in the energy consumption. However, they have shown to provide better efficiency [7, 8]. Extensive parametric studies were performed for fluidic VG jets [9, 8, 10, 11] to optimize geometrical and actuation parameters. When they are inclined compared to the wall and the flow direction, VG jets generate streamwise longitudinal vortices, bringing high-momentum flow closer to the wall and moving away low-momentum flow from the wall [12]. The vortices strength (related to for example the velocity ratio $VR = U_j/U_0$, with U_j the jets output velocity) increases the penetration height of the jet through the boundary layer [7, 13] and looses in intensity by convecting downstream [8]. Arrays of fluidic VG jets aligned on the spanwise direction have been found to generate a corresponding array of streamwise vortices which interact together [14, 15]. Co-rotating VG jets (when all the jets are aligned in the same direction) produce co-rotating longitudinal vortices convecting spanwise with a global displacement [14]. In order to reduce the flow rate injected and to interact with the unsteady dynamics of the natural flow field, pulsed actuation is generally introduced [16]. For similar conditions of actuation, better efficiency was observed by using pulsed control [17, 18]. Compared with continuous actuation for which only the velocity ratio (VR) is modified, pulsed control offers a larger range of parameters (frequency f, and duty cycle DC typically) and, therefore, a wider range of control actuation strategies. For a flow under actuation, while the steady

*Corresponding author
Email address: support@elsevier.com (C. Raibaudo)

Study	**System**	**Actuator**	**Sensor**	**Controller**
[27]	Hump	FV	Pressure	PID
[28]	BFS	LS	Pressure	$\mathcal{H}_\infty$, Smith predictor
[29]	BFS	LSs	Pressure	$\mathcal{H}_\infty$
[30]	Airfoil	ZNMF	Balance	Simplex optimization
[31]	Airfoil	FV	Pressure	Extremum/slope-seeking
[32]	D-shaped body	LS	Pressure	Extremum-seeking
[33]	Airfoil	DBD	Balance	Slope-seeking
[34]	Airfoil	DBD	Hot-films	Direct feedback
[35]	Airfoil	FV	Hot-films	Direct feedback
[25]	Ramp	FV	Hot-films	PID, LQR
[36]	BFS	FV	RT PIV	PID, Gradient
[37]	Multiple experiments			Genetic programming
[38]	Airfoil	DBD	Pressure	Deep Reinforcement Learning
[39]	Airfoil	ZNMF	Pressure	PI
Present study	**Ramp**	**FV**	**Hot-films**	**PID, LQR, LQG,** $\mathcal{H}_\infty$

Table 1: Closed-loop experimental flow control studies in the literature. BFS: backward-facing step, DBD: Dielectric barrier discharge, FV: Fluidic valves, LS: Loudspeaker, RT PIV: Real-Time Particle Image Velocimetry, ZNMF: Zero-Net Mass Flow jets.

regime gives indication on the performance of the controller implemented, the transient regime is also of particular importance for the optimisation of this controller. The transient dynamics of reattachment must, therefore, be also characterized and modeled. The dynamics of separation and reattachment for two-dimensional separation flows under control have been investigated for cylinders [19], mixing layers [20], flat plates [21], airfoils and bluff bodies [22, 23, 24, 25, 26] and is generally quantified by a characteristic time response τ. When scaled by the separation length L_{sep} and the freestream velocity U_0, the reduced time scale $\tau^+ = \tau U_0/L_{sep}$ is generally found to range between 5 and 10 for reattachment [22, 24, 20, 26], and between 14 and 25 for separation [22, 21, 24, 20] regimes.

In addition, active actuators offer the capability to realize closed-loop control. Feedback control has gained interest in the past few years, in particular in perspective of industrial applications and rejection of disturbances. When the flow is subject to incoming perturbations, only a closed-loop controller is able to maintain the control performance if it is said robust [28]. A non-exhaustive list of closed-loop experiments for flows achieved in the past is presented in Tab. 1. Only experimental literature is shown here, but numerical investigations can also be found for cylinders [19, 40], cavities [41, 42] or ramps [43] for example. A numerous number of possibilities have been tested, in terms of flow configurations (backward-facing step, airfoils, ramps...), types of actuators (fluidic, synthetic jets, plasmas...), sensors (pressure, friction, lift-to-drag ratio...) and feedback controllers in particular.

Direct feedback control laws have been used due to their ease of implementation. These are based on a precision criteria between a reference value and the controlled variable (for [34] and [35], the shear stress measured by hot-film sensors). In particular, PID regulators are still considered in control community as canonical controllers. In [27], the authors conducted experimental closed-loop control of a hump model driven by oscillatory pressured valves using PID controller. The fluctuating wall-pressure along the model was considered as the controlled variable. In [36], a similar controller was used to reduce the length of the recirculation region downstream of a backward-facing step using real-time PIV snapshots. Again, in [25] reattachment of a separated boundary layer on a 2D ramp was obtained thanks to a PID controller. In the latter, the friction signal of hot-films sensors was used as input variable and the duty cycle of the pulsed fluidic VG jets as the output variable of the controller. Compared to open-loop tests, a significant improvement of the control reactivity was observed and a reduction of mass flow injected of nearly 20 % was achieved.

Adaptive control was also used for flow control as an interesting advanced technique. Extremum and slope seeking have been considered in particular in the past. These algorithms allow an optimization of the control without knowing the cost function or the plant optimum value. Tian et al. [30] realized adaptive closed-loop control using the simplex method to minimize the drag-to-lift ratio for an airfoil under synthetic jets. Best results show lift-to-drag ratio 5 times higher than the uncontrolled baseline flow. Pastoor et al. [32] used slope-seeking technique to reduce the drag of a D-shape body. The average drag was reduced by 15 % with a 40 % base pressure increase, compared to the baseline flow. Benard et al. [33] used the same slope-seeking technique for an airfoil under plasma DBD control. A force balance measuring the lift was used as the control gain estimation. Performances similar to the open-loop parametric investigation are obtained with adaptive closed-loop control with minimal voltage. Robust control for flow control on airfoils and bluff bodies is still under investigation. The robust synthesis is difficult to design due to the difficulties to extract complete dynamics of the system and to quantify the uncertainties of the plant inputs and outputs. $\mathcal{H}_\infty$ synthesis was mostly employed in the past as a reference robust controller. Becker et al. [28] used two $\mathcal{H}_\infty$ controllers for a backward-facing step configuration under speakers slots control. Compared with a Smith predictor loop and to open-loop results, the average velocity of the command is 52 % higher, but the controller responds faster and more robust to drastic changes in the reference value. Henning et al. [29] used the same experimental set-up using multiple pressure sensors donwstream the step. Despite a lower dynamics due to the RMS-based criteria, the $\mathcal{H}_\infty$ synthesis provided high precision and robustness to changes of the reference command. Shaqarin et al. [25] developed $\mathcal{H}_\infty$ and Linear Parameter-Varying controllers from experimental hot-film sensors data to increase the closed-loop control performances with high variations of the wind-tunnel velocity.

~~Considering robust control is fundamental for real applications. Controllers have to resist to abrupt changes of the incoming boundary layer or uncertainties on flow model. Robust flow control is however understudied. A comparison with other standard closed-loop controllers is also important to investigate for a given experimental set-up. Theoretical performances of each controller has to be verified. The objective of the present study is thus to achieve robust control by increasing step by step the complexity of controllers. The flow configuration retained here is that of the 2D ramp used by the previous studies.~~ *The main objective of the present study is a comparison of different closed-loop controllers, all implemented for one experimental set-up of flow control. Their performances – precision, optimality with respect to the cost, influences of the noise and uncertainties – are here compared using the same flow conditions, actuators and sensors configuration, already used and well documented in previous studies [11, 25, 26]. The complexity and performances expectations of the feedback controllers increase gradually, from linear regulator to robust control, proving for each solution their benefits. Robust control in particular is studied here as an important potential for flow control strategies on applied systems.* The overall experimental set-up is presented in section §2. The main characteristics of the natural separated flow is presented in section §3, and open-loop results are discussed in section §4 to obtain models of the flow transients under actuation. The different models investigated are detailed in section §4. Closed-loop control using PI (§5.1), LQR and LQG (§5.2) and robust $\mathcal{H}_\infty$ (§5.3) controllers is presented in section 5.

2. Experimental facilities

2.1. Wind-tunnel and ramp model

The experiments presented in this study were realized in the closed-loop boundary layer wind-tunnel at the Laboratoire de Mécanique de Lille. A 20 m long section with constant area of $2m \times 1m$ allows the boundary layer to develop. The maximum freestream velocity and the turbulence level were $U_\infty = 10$ m/s and 0.03% respectively. Full details on the wind tunnel and the flow characteristics can be found in Carlier et al. [44].

Beyond 14.4 m from the beginning of the test section, a two-dimensional ramp is mounted. A scheme is presented in figure 1. The ramp is constituted of four parts: (i) a convergent part with a contraction ratio of 3/4, (ii) an articulated flat plate of 2.14 m in length with an angle of $\alpha_R = -2°$ relative to the wind-tunnel floor, (iii) an articulated flap of 0.34 m in length with an angle of $\beta_R = -22°$ and (iv) a flexible plastic sheet to ensure a smooth connection to the floor of the wind tunnel. The ramp height H_s is 17.5 cm at the leading edge of the flap.

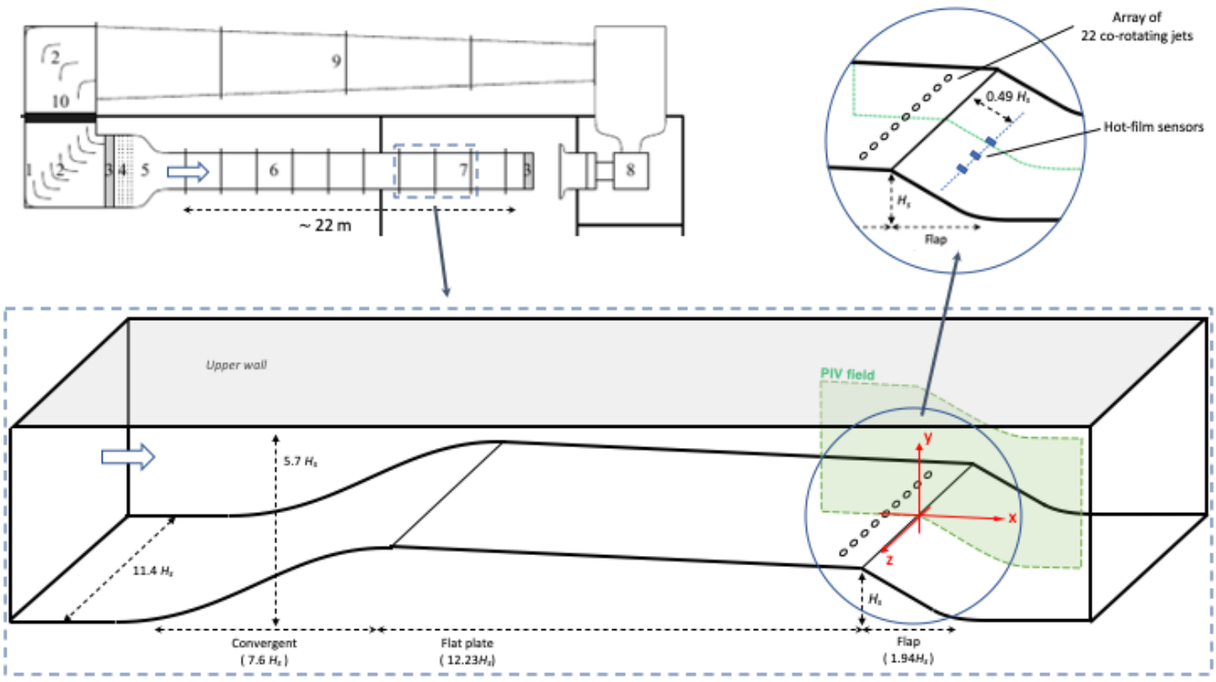

Figure 1: (Top-left) Boundary layer wind tunnel at Lille (France) where te tests have been conducted with (1) plenum chamber, (2) guide vanes, (3) honey-comb, (4) grids, (5) convergent, (6) boundary layer developping zone, (7) test section, (8) fan and motor, (9) return circuit. (Bottom) Schematic of two-dimensional located in the test section. (Top-right) Location of the co-rotating jet and Senflex SF9902 hot-film sensors.

At a freestream velocity of $U_\infty = 10$ m/s, the boundary layer thickness at the leading edge is $\delta = 0.19$ m, the momentum thickness $\theta = 0.0165$ m and the local reference freestream velocity, *chosen at the separation position and higher than the incoming velocity due to the contraction, is* $U_0 = 12.3$ m/s . The Reynolds number based on momentum thickness Re_θ is 20600. The leading edge of the flap is used as origin of spatial coordinates as specified in figure 1. Full details on the ramp characteristics can be found in Cuvier et al. [11].

2.2. Control set-up

Controlling the separated flow needs actuators integrated in the plant (§2.2.1). Model-based closed-loop control is also a critical consideration for the present study, as stated in the introduction. To achieve this objective, a real-time estimation of the flow state is required using instantaneous sensors. Spatial measurements of the flow during the transient were performed with PIV, in addition to these instantaneous signals, to complete the model (§2.2.2). Both actuators and sensors were used to design and applied closed-loop controllers (§2.2.3).

2.2.1. Actuators

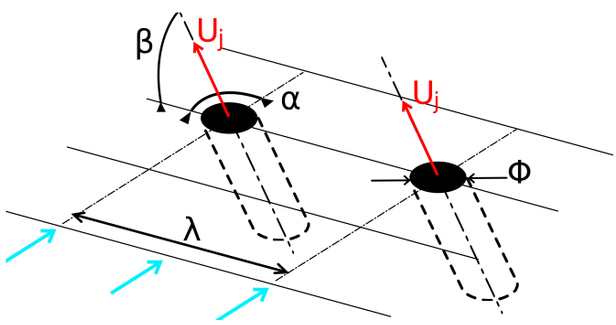

Figure 2: Co-rotating configuration of the actuators used in this study. $\alpha = 125°$ the skew angle, $\beta = 35°$ the pitch angle, $\phi = 0.03\ \delta$ is the diameter, $\lambda = 13.6\ \phi$ the spacing between two jets [26].

An array of $N_j = 22$ co-rotating round jets of $\phi = 0.03\ \delta$ in diameter and located at $\Delta X_{vg} = 47\phi$ upstream the separation line is distributed spanwise and used for actuation. Air is supplied to Festo solenoid valves by a 75 kW compressor through a first reservoir of 2 m^2 and a secondary 0.09 m^2 tank which absorbs pressure variations. The flow rate of the valves is fixed by sonic throats with $S_c = 1.3$ mm^2 cross section. The solenoid valves were driven electrically and controlled by an Arduino micro-controller. The actuation apparatus suggested by Braud et al. [45] and implemented by Shaqarin et al. [25] is used here. The jets were blowing in the upstream direction

with a skew angle of $\alpha = 125°$ and a pitch angle $\beta = 35°$ *, as presented in Fig. 2 and in Raibaudo et al. [26]* . This configuration was selected as corresponding to the optimal configuration among the ones tested by Cuvier et al. [11]. The spacing between two consecutive jets is $\lambda = 14.3\ \phi$. An average dispersion of 4.8 % in the jets outlet velocity was observed and can be attributed to the tolerance in sonic throat diameters. The temperature at the jets exit was also measured and a difference of 1.2 $°C$ was observed whatever the actuation parameters. In the perspective of closed-loop control, it is important to ensure that the time response of the actuators is siginificantly lower than the characteristic times of reattachment and separation. In complement of the studies of Kostal et al. [14] and Braud et al. [45], who used the same set-up, the jet exit velocity response was measured under continuous actuation by hot-wire anemometry [26]. At the valves opening, an overshoot of velocity followed by oscillations is observed. These oscillations are due to an acoustic shock wave propagation as described by Braud et al. [45]. The velocity then reaches a steady value after a non-dimensional time delay $t^*_{dj} = t_{dj} U_0 / H_s$ of approximatively 0.6. This time delay was found much lower than the characteristic times associated with flow reattachment as discussed further.

For a fixed air pressure supply, the actuators can be driven in frequency f and duty cycle DC. These two control parameters affect the actuation cost, or again the mass flow rate injected, which can be expressed as a non-dimensional momentum coefficient c_μ defined, on a period of actuation, as:

$$c_\mu = \frac{DC\ (\rho_j\ U_j^2\ S_j)}{(0.5\ \rho_0\ U_0^2\ \delta\ \lambda)} \tag{1}$$

where ρ_j the air density at the jets exit, ρ_0 the air density of the free stream, S_j the jet exit area. The actuation cost can thus be seen to be proportional to the duty cycle DC. This motivates therefore the choice of DC as the control variable $u(t)$ in the closed-loop experiments presented further (Fig. 3). In the following, the actuation frequency is expressed with a non-dimensional reduced frequency $F^+ = f L_{\text{sep},0} / U_0$ with $L_{\text{sep},0}$ the separation length for the unforced flow. A jet to freestream velocity ratio of $VR = 5$ is considered in the present study. *In the previous work [46], with different velocity ratios VR tested in open-loop, the controlled flow state – i.e. the flow state after the transient start of actuation – was not considered stable for $VR \leq 3$. The evolution in time of the separation area for example was found to be stabilized long after the actuation beginning for $VR = 5$, but not for $VR = 3$ [46]. Therefore, a velocity ratio VR of 5 is chosen to ensure a stable controlled flow state, necessary for the closed-loop control, and to use the documented open-loop characterization performed at this velocity ratio.*

2.2.2. Metrology

Two-dimensional two-component (2D2C) phase-averaged PIV measurements were performed in a streamwise/wall-normal plane for the open-loop characterization of the transient dynamics of the reattachment. The measurement plane, presented in figure 1, was located at the wind-tunnel middle ($z = 0$), midway between two jets. Four Hamamatsu cameras with a resolution of 2048×2048 px^2 were installed to cover the overall region of study, which comprises: the incoming boundary layer not yet separated located upstream the leading edge, the separation bubble and the reattachment region downstream the ramp. The entire field of view is 5δ in length and 1.5δ in height. Nikon lenses with a focal of $f_o = 50$ mm were set on the cameras. The optical apparatus is fully detailed in Cuvier et al. [11]. A laser sheet of about 8 mm thick was realized using a Nd-Yag Laser with an energy of 400 mJ per pulse. The laser reflection on the wall was reduced using a rhodamine paint developed by ONERA (Office National de Recherches en Aérospatiales) applied along the laser sheet position. The time separation between two laser pulses is fixed at $\Delta t = 80\ \mu$s to minimize the out-of-plane motion, considering the laser sheet thickness. A free-stream displacement of about 6-7 pixels is estimated for the present experiment. PIV images were acquired at 4 Hz and processed using an in-house software (adapted by Cuvier et al. [11] from the MatPIV 1.6.1 toolbox written by J.K. Sveen) using standard multi-grid/multi-pass cross-correlations algorithm with a final spatial resolution of 1.5×1.5 mm^2. One pass with a 64×64 px^2 interrogation window and three passes with a 32×32 px^2 interrogation window were performed, with a overlapping of about 70 %. The PIV measurement uncertainty described by Foucaut et al. [47] is estimated using the merging regions. Maximal random errors of 0.25 px far from the wall and 0.7 px near the wall were obtained, then decrease along the ramp.

An array of hot-film sensors (Senflex SF9902) was distributed on the flap to survey the skin friction behaviour during reattachment, simultaneously to the PIV acquisition. The sensitive part of the sensors is 1.5 mm long and

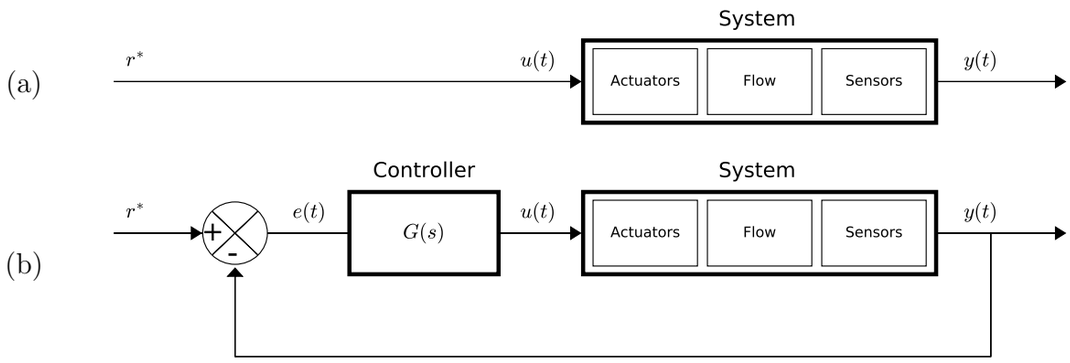

Figure 3: Designs of the (a) open-loop and (b) closed-loop strategies. r^* is the target, $u(t) = DC(t)$ the command signal (here the duty cycle), $y(t) = E(t) - E_0$ the output signal (here the friction gain), $e(t) = r^* - y(t)$ the error signal, $G(s)$ the transfer function of the controller.

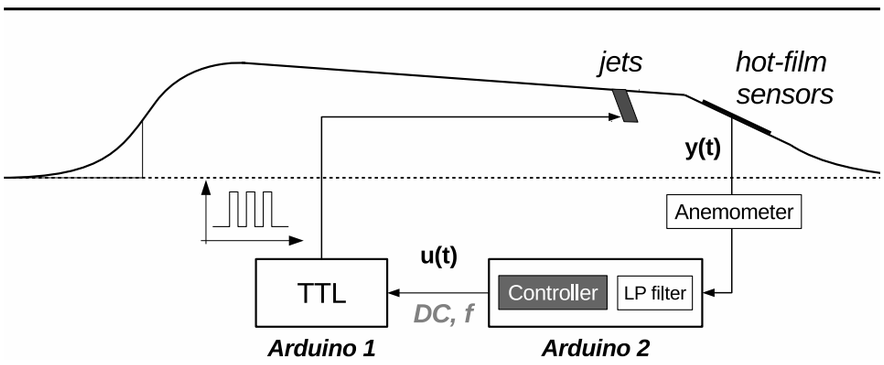

Figure 4: Experimental closed-loop setup. The first Arduino card generates the signal for the valves, the second Arduino card provides the duty cycle and the frequency from the input friction gain and the command low from the controller.

0.1 mm wide. The sensors are deposited on a polyamide substrate with a thickness less than 0.2 mm and were connected to an AN1003 constant anemometer manufactured by AAlab Systems. *Note that the raw output voltage $E(t)$ of the hot-film sensors is considered in the closed-loop control scheme detailed in the next sections. The wall shear stress is proportional to $E^6(t)$ and applying a calibration might therefore be intuitive. However, calibration of hot-film sensors is delicate. Futhermore, previous authors have demonstrated that the raw output voltage can be directly used to detect and control flow separation (Seifert & Pack-Melton [48], Poggie et al [49], Mathis et al [50], Chabert et al [51]). As the operating range of sensors is small, the sensitivity of sensors is limited and can be used for flow control for this present configuration.* Hot-film signals were sampled at 10 kHz. A detailed study about the characteristic times of the controlled flow dynamics obtained from each hot-film sensor can be found in Raibaudo et al. [26]. The three hot-film sensors used in the current study are aligned in the spanwise direction $x/H_s = 0.49H_s$ downstream of the separation and at $z/H_s = (-0.46,\ 0.35, 0.12)$. *The drift in temperature of the wind-tunnel does not exceed $\pm 0.2°C$ thanks to regulation. The drift in the output voltage during the experiments was consequently observed to be limited.*

2.2.3. Closed-loop set-up

The control set-up is summarised in figure 3, for (a) open-loop and (b) closed-loop strategies. As mentioned previously, the duty cycle is used as the command variable $u(t) = DC(t) \in [0, 100]\%$. The friction gain, defined as the difference between the instantaneous signal output of the hot-film $E(t)$ and its time-averaged value for the uncontrolled flow E_0, is considered as representative of the flow state during the reattachment and separation process and is therefore chosen as the output variable of the plant $y(t) = E(t) - E_0$.

Two Arduino cards were used as presented in figure 4. The first Arduino acquires the hot-film sensors and calculates the static error defined as $e(t) = y(t) - r^*$ (with r^* a user-defined target) used by the second Arduino to update the closed-loop controller command $u(t)$ which is driving the actuators. Two separated cards were preferred to ensure fast calculations of the control law and precision for the output signal generation.

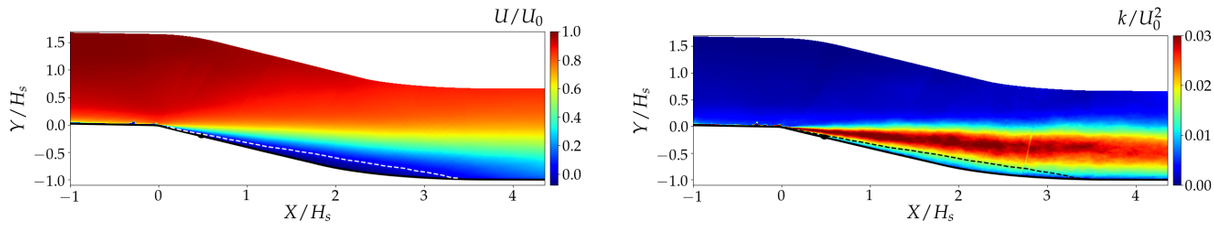

(a) (b)

Figure 5: Spatial distribution of (a) the average streamwise velocity field $\overline{U}\ /\ U_0$ and (b) the turbulent kinetic energy $k\ /\ U_0^2 = \frac{1}{2}\left(\overline{u'^2} + \overline{v'^2}\right)\ /\ U_0^2$ for the un-controlled flow. Continuous line: wall; dotted line: mean separation line detected by the χ criterion; black circle: streamwise position of the hot-wire sensors.

3. Baseline flow

A description of the mean flow field for the uncontrolled flow, obtained from PIV, is given in figure 5. The mean streamwise velocity and the turbulent kinetic energy, scaled by the streamwise mean velocity measured at the leading edge far from the geometry ($U_0 = 12.3$ m/s), are shown in Figure 5(a) and 5(b) respectively. ~~The average separation region is detected using a backflow coefficient χ of 0.5 as proposed by Simpson [52] leading to a separation bubble which start at $0.1H_s$ downstream the leading edge with a length $L_{sep,0}$ of about $3.4H_s$.~~ *The mean separation bubble is determined using the backflow coefficient χ, proposed by Simpson [52], as the ratio in samples of reverse flow, compared to the total of available samples. A backflow coefficient χ of 0.5, named by Simpson as "transitory detachment", is used for the separation line detection. The total separation bubble corresponds to a backflow coefficient $\chi \leq 0.5$. It leads to a separation bubble starting at $0.1H_s$ downstream the leading edge with a length $L_{sep,0}$ of about $3.4H_s$.* The flow is two-dimensional over 70% of the flap span. Near the side walls, side wall effects were observed thanks to surface oil visualisations not reported here for conciseness. A detailed description of the baseline flow can be found in [26].

4. Plant modelling

Performance of closed-loop control in terms of optimality and robustness depends on both the controller itself and the model of the plant. Open-loop experiments were thus performed for modelling the transient response of the plant during reattachment and separation phases. To obtain an averaged picture of the flow transients under actuation, phase-averaging is considered for successive periods of continuous actuation. During two successive periods of jets blowing, the actuation is turned off to let the flow naturally return to its separated state. Two models to represent the flow state are considered. The first one uses the friction gain response as a local representation of the flow while the second model uses the recirculation length as a global variable. The latter is further combined with a Kalman filter to take into account measurement and process noises. Note that the model identification is performed on the basis of a continuous forcing of the flow. As reported in [26], transient responses with similar characteristics have been observed when pulsed actuation is used. Note also that the transient models used here are linear but can be used with nonlinear controllers [25].

4.1. Model A: Transient model of the friction gain

The phase-averaged response to a step of the non-dimensional friction coefficient $x^*(t) = (E(t) - E_0)\ /\ (E_\infty - E_0)$, where E_∞ is the steady value reached by the hot-film signal is presented in figure 6. The phase-averaged response is computed with $N_c = 500$ repeated cycles of forcing/unforcing regimes (5 seconds each). The continuous black line corresponds to the phase-averaged hot-film response to the jets driven by the command signal $u(t)$ shown in continuous gray line. The actuation is turned on at $t = 0$. The friction gain first increases, suggesting some flow reattachment, before reaching a stationary value representing the steady controlled regime at $t \sim 200H_s/U_o$. *It should be noted that, at the transient start, the hot-wire sensors are showing positive gain when they are still in the separation bubble and could lead to a non-linear response to the control. However, and in particular for the first line of sensors (including S_1), when applying the control, the separation point is rapidly pushed downstream. Linearity of the response is valid after this short delay.* When the actuators are turned off ($t \sim 350H_s/U_o$), the friction gain rapidly decreases to reach the value for the separated state. A time delay t_d between the hot-film response

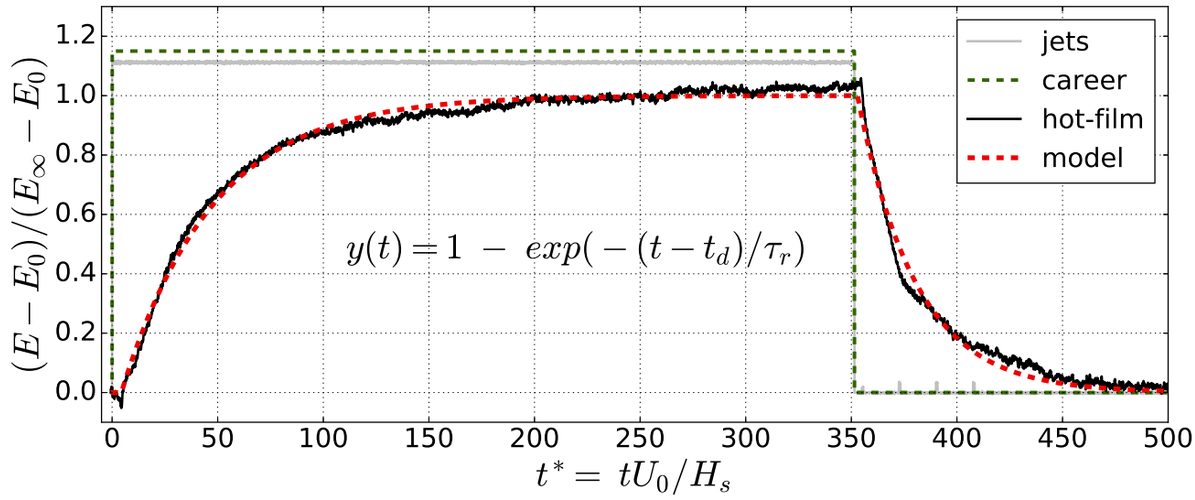

Figure 6: Friction gain response to continuous actuation (velocity ratio $VR = 5$, freestream velocity $U_\infty = 10$ m/s) for the hot-film sensor S_1 located at $X/H_s = 0.49$ from the leading edge of the flap and at $Z/H_s = -0.46$ from the centered line. (green dotted line) actuation career period, (gray line) actuation signal, (black line) friction gain, (red dotted line) first-order model fitted on the friction gain response.

and the command signal was observed when the actuation is both turned on and off. As detailed in [26], this time delay is representative of the convection time needed by the co-rotative structures generated by the jets to reach the streamwise position of the hot-film sensor. The transient response to a step command $u(t)$ of the friction gain $x(t) = E(t) - E_0$ during separation and reattachment regimes is found to be well described by a first-order response with delay [25]. The state-space representation for the regime of reattachment can thus be written as:

$$\dot{x}(t) \quad = \quad -(1/\tau_r) \quad x(t) \quad + \quad (E_\infty - E_0)/\tau_r \quad u(t - t_d) \tag{2}$$

with τ_r the characteristic rising time. Note that E_∞ and t_d depend on the DC and actuation velocity ratio as previously shown by Shaqarin et al. [25]. For further implementation of the model in closed-loop control, these values are identified using a pseudo calibration procedure as detailed in Raibaudo et al. [26]. The procedure consists in initially forcing the flow to one period of continuous actuation and to identify the two quantities prior to turn on the controller. For the present set of control parameters (continuous actuation, $VR = 5$), a time delay $t_d = 3.9H_s/U_o$ and a characteristic time for reattachment $\tau_r = 21.1H_s/U_o$ were found comparable with the ones reported in literature [21, 20, 24].

4.2. Model B: Transient model of the recirculation length

The friction gain measured by a single hot-film sensor provides only a local representation of the flow behavior. Several authors suggested to use a measure related to the recirculation region, such as the recirculation area or length, which represent a global variable believed to be more appropriate to represent the flow dynamics [53, 54, 36]. The recirculation length is here retained. The later is computed thanks to the phase-locked PIV measurements performed and described in section 2.2.2. Considering $\mathbf{u}(\mathbf{x}, t_k)$ the instantaneous velocity vector at phase instants t_k, the phase-averaged velocity vector $\widehat{U}(\mathbf{x}, t_k)$ can be expressed as:

$$\widehat{U}(\mathbf{x}, t_i) = \frac{1}{N_c} \sum_{n=0}^{N_c - 1} \mathbf{u}(\mathbf{x}, t_i + n/f) \tag{3}$$

where N_c is the number of repeated cycles of actuation over which the average is effected, and t_i a time delay introduced for phase discretisation. Snapshots of the phase-averaged streamwise velocity component computed by the last equation are reported in figure 7. The phase location in the phase-averaged response of the friction gain is also reported at the bottom left of each subfigures. During the sequence reported, the separation bubble shows no modification compared to the baseline flow until $t = 3.5H_s/U_o$. Considering the time delay observed on the hot-film response ($t_d = 3.9H_s/U_0$ in figure 6), the co-rotating structures generated by the actuation are not convected yet to the separation region. However, penetration of the structures into the boundary layer is manifest in the region upstream of the leading edge of the flap where a third of the boundary layer thickness is shown to be affected. From $t = 3.5H_s/U_o$, the separation point is first pushed downstream while the reattachment point

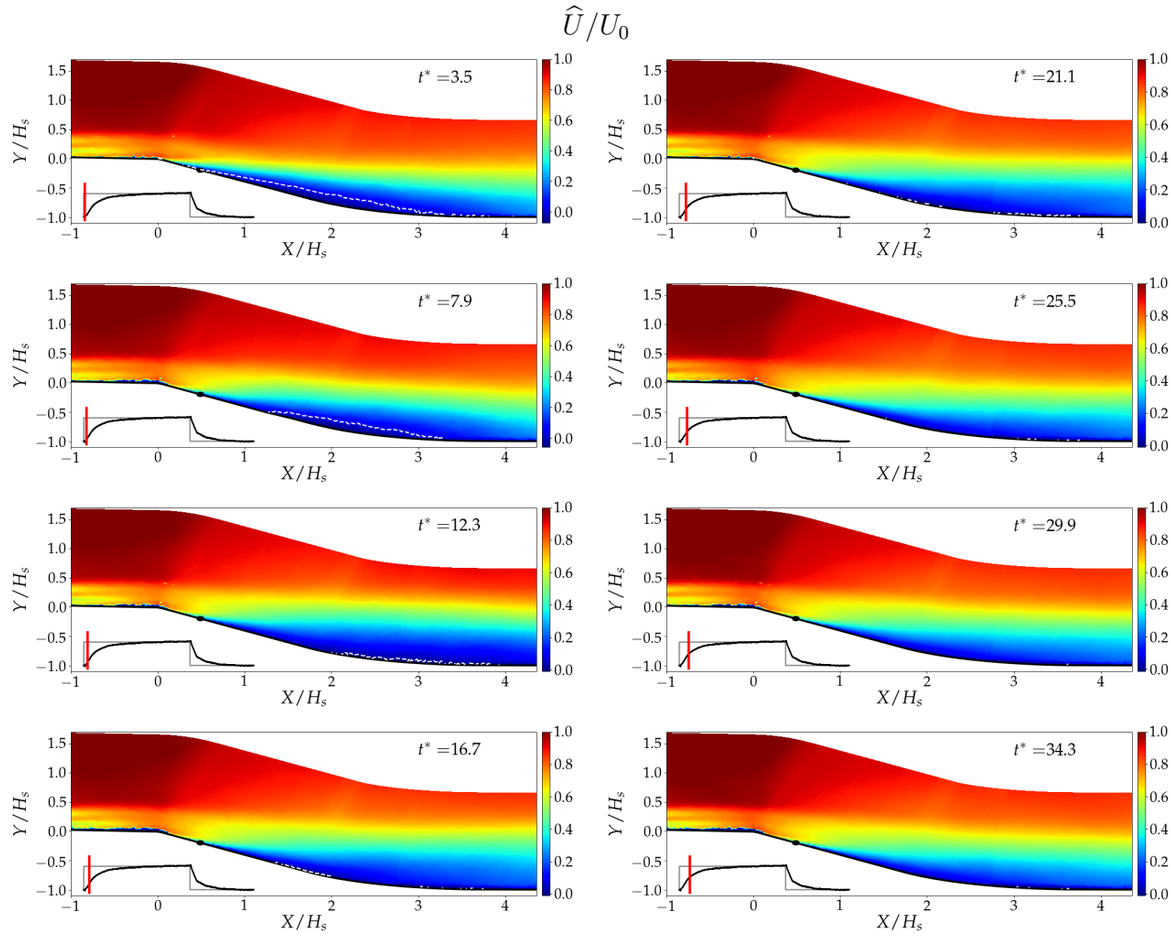

Figure 7: Evolution of the phase-averaged streamwise velocity $\widehat{U}/U_0$ for a stabilized flow with continuous actuation (U_∞ = 10 m/s, $VR = 5$) for succesive phase instant $t_i^* = t_i U_0/H_s$. The thick continuous line corresponds to the wall, the dotted line to the mean separation line detected by the χ criteria, the black circle to the streamwise position of the hot-wire sensors.

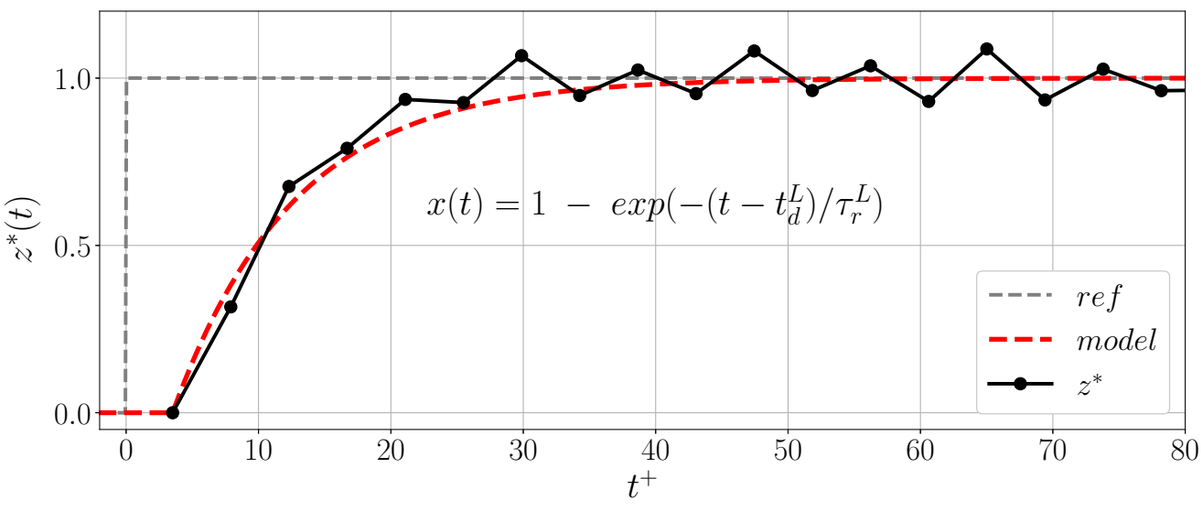

Figure 8: Phase-averaged response of the normalised reduction of the separation length $z^*(t) = (L_{sep,0} - L_{sep}(t))/(L_{sep,0} - L_{sep,\infty})$ to continuous actuation: (Gray line) actuation signal, (black line) separation length reduction, (red dotted line) first-order model.

remains at $X/H_s \sim 3.3$. The bubble is then flattened drastically, then mostly reduced for $t > 16.7H_s/U_o$. Tiny pockets of separated flow appear in the separation region (around $X/H_s = 1.5 - 2$ and > 3), but can be hardly observed for $t > 29.9H_s/U_o$. It should be noticed that the friction gain continues to increase after $t = 34.3H_s/U_o$, whereas the phase-averaged streamwise velocity seems to reach a stationary regime [26].

To model the transient dynamics of the separation length $L_{sep}(t)$, derived from the phase-averaged velocity field discussed previously, a gain in separation length can be defined, similarly to the friction gain, as $x^L(t) = L_{sep,0} - L_{sep}(t)$. An increase of $x^L(t)$ corresponds to a reduction of the separation length. The phase-averaged response to continuous actuation of the non-dimensional coefficient $x^L(t)/(L_{sep,0} - L_{sep,\infty})$, with $L_{sep,\infty} = 0.49H_s$ the mean separation length for the stationary reattached flow, is shown in figure 8. The actuation signal is plotted in gray, the phase-locked separation length coefficient in black. Similarly to the friction gain, the phase-averaged

response of the gain in separation length is found to be well modelled by a first-order response with delay. The state-space representation can be written as:

$$\dot{x^L}(t) \quad = \quad -(1/\tau_r^L) \quad x^L(t) \quad + \quad (L_{sep,0} - L_{sep,\infty})/\tau_r^L \quad u(t - t_d^L) \tag{4}$$

with τ_r^L the characteristic time for the separation length and t_d^L the time delay observed for the separation length dynamics. The characteristic time $\tau_r^L = 9.1 H_s/U_0$ is found lower than the one obtained for the friction gain and confirms the previous observations on the velocity fields. In contrast, the time delay $t_d^L = 3.5 H_s/U_0$ is found similar to that observed for the friction gain ($t_d = 3.9 H_s/U_0$). The later again corresponds to the convection time of structures generated by the actuation to reach the separated region.

4.3. Model C: Model-based estimate of the recirculation length

The separation length provides an appropriate metric for the measurement of the control efficiency but is difficult to access in real-time. In contrast, the friction gain is accessible instantaneously but is generally perturbed by noise with significant level. This noise can be responsible of performance decrease of the controller [55]. A steady-state Kalman filter approach is considered to build an optimal linear estimator of the separation length. The dynamical model for the separation length can be written as the following time-invariant model,

$$\left\{ \begin{array}{rcccccccc} \dot{x}^L(t) & = & -(1/\tau_r^L) & x(t)^L & + & (L_{sep,0} - L_{sep,\infty})/\tau_r^L & u(t - t_d^L) & + & v(t) \\ \mathbf{y}(t) & = & H_{yx} & x^L(t) & & & & + & w(t) \end{array} \right. \tag{5}$$

where $v(t)$ and $w(t)$ are stochastic disturbances considered as Gaussian white noises, with zero-mean and known covariances $Q_{v,v}$ and $Q_{w,w}$ respectively. The second equation is known as the measurement equation and relates the measurement variable $\mathbf{y}(t) = [y_1(t), y_2(t), y_3(t)]^\intercal$, which includes the value of the friction gain measured by the three hot-film sensors, to the state variable x^L through the linear mapping H_{yx}. The latter is given by the vector $[\alpha_{y_1 x}, \alpha_{y_2 x}, \alpha_{y_3 x}]^T$ and identified *a priori* from data obtained for the baseline case. The measurement and process covariances are calculated based on the variances (for the baseline flow) of, respectively, the instantaneous velocity PIV data in the region between the separation point and the sensors, and the hot-film signals for the baseline flow. This results in $Q_{v,v} = 2.23$ m^{2}s^{-2} and $Q_{w,w} = 1.02\mathbb{I}_3$ V^2 with $\mathbb{I}_3 \in \mathbb{R}^{3\times3}$ the identity matrix. These values are, arbitrarily, overestimated as the controlled flow usually shows lower signal variance. Following the standard procedure, the optimal solution $\widehat{x}^L$ of the estimation problem is approximated by,

$$\left\{ \begin{array}{rcccccccc} \dot{\widehat{x}}^L(t) & = & -(1/\tau_r^L) & \widehat{x}^L(t) & + & (L_{sep,0} - L_{sep,\infty})/\tau_r^L & u(t - t_d^L) & + & \mathbb{L}(\mathbf{y}(t) - \widehat{\mathbf{y}}(t)) \\ \widehat{\mathbf{y}}(t) & = & H_{yx} & \widehat{x}^L(t) & & & & & \end{array} \right. \tag{6}$$

with $y(t) - \widehat{\mathbf{y}}(t)$ the observation error and $\mathbb{L}$ the optimal gain determined by solving the continuous-time algebraic Ricatti equation associated with the system of Eq. (6) [56]. The interest of such estimator for control purpose will be discussed later in section 5.2.2.

5. Closed-loop control

Results for the closed-loop experiments are presented in this section. Different closed-loop controllers are considered to achieve different objectives –reaching particular target of the output signal, reducing the control cost or the output noise, or again increasing the robustness of the control– and their performances are compared in an attempt to provide some guides for future turbulence control efforts.

From now on, pulsed actuation is considered. The actuation frequency is maintained fixed and equal to the theoretical optimal frequency $F_{opt}^+ = 1$ [57, 58, 59]. As discussed in section 2.2.1, the duty cycle DC is considered as the unique control variable. The target value is chosen to be reachable by the controlled system, but not too close to the actuation capabilities limits. To compare the performances of the different controllers tested, the following results are presented according to the same figure format: subfigure (a) will show the friction gain $E(t) - E_0$ and the corresponding first-order model fitted on data, while subfigure (b) will show the duty cycle $DC(t)$ (control law) during the control period. The steady regime is considered reached for $t > 210 H_s/U_0$. During this regime (indicated with an horizontal arrow in the subfigures), averaged steady friction gain $E_\infty - E_0$, the duty cycle DC_∞, and the characteristic rising time τ_r^* were measured and indicated in the figures.

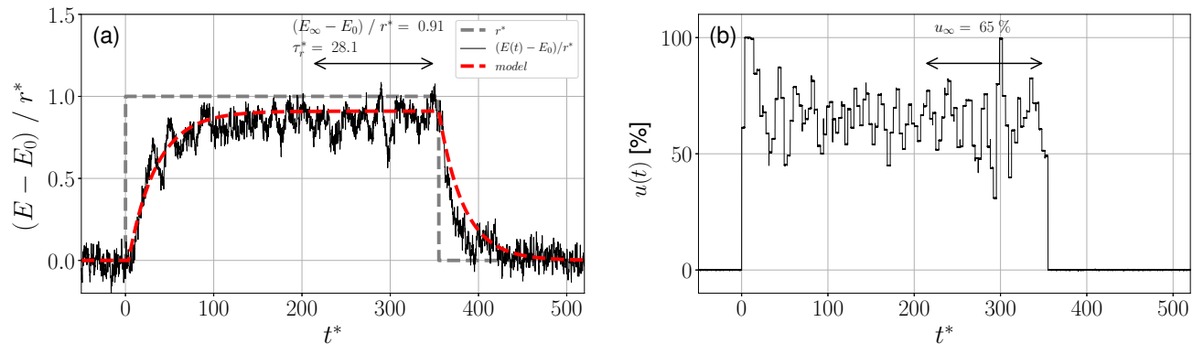

Figure 9: Results for PI controller. (a) friction gain $E(t) - E_0$ and corresponding steady value $E_\infty - E_0$ and characteristic time τ_r^*, (b) duty cycle $DC(t)$ and corresponding steady value DC_∞.

5.1. Regulation with PI controller

A Proportional-Integral (PI) controller is first implemented for the plant modelled by equation (2). In control theory, this controller is generally considered as a reference case. The objective of the controller is to minimize the error $e(t) = y(t) - r^*$ between the target value r^* and the measurement variable $y(t)$ by applying a control law for $u(t)$ based on proportional and integral terms of the error. This can be expressed as:

$$u(t) \;=\; k_p\, e(t) \;+\; k_i \int_0^t e(\tau)\, d\tau \tag{7}$$

with k_p and k_i the coefficients for proportional and integral terms respectively. Thanks particularly to the integral term, PI controllers were theoretically designed to cancel the static error $e_\infty = r^* - y_\infty$. Parameters k_p and k_i, which are model-dependent, have to be tuned properly to achieve a given performance in terms of time response and static error. The empirical tuning technique of Ziegler-Nichols in open-loop [60] is here implemented for convenience to obtain satisfactory coefficients. In this method, only proportional control is used for tuning. The gain is increased up to the critical or ultimate gain for which the output shows sustained oscillations. Given the model of equation (2), the coefficients of the PI controller are given by [60],

$$\left\{ \begin{array}{rcl} k_p &=& 0.9\tau_r/(E_\infty - E_0)t_d \\ k_i &=& k_p/3.3t_d \end{array} \right. \tag{8}$$

Results for this controller are presented in figure 9. A value or r^* corresponding to 80% of the achievable friction gain obtained in open-loop control with continuous blowing is considered. Note that other tests were conducted with other values and the results revealed similar trends than that describe below. Once the controller is activated, the friction gain response (Fig. 9(a)) follows a first-order trend before reaching a mean value of $0.9r^*$. Significant fluctuations are noticeable for the measured friction gain and command law $u(t) = DC(t)$ found by the controller. The evolution of DC, reported in figure 9(b), first exhibits an overshoot up to 100 % before converging to a mean value of $u_\infty = 60$ % with fluctuating values between 0.52 u_∞ and 1.54 u_∞. Compared to a proportional controller (not presented here for conciseness but detailed in Raibaudo [46]), the static error was found to be significantly reduced ($0.09r^*$ compared to $0.36r^*$ for the P controller). The large fluctuations of DC and the remaining static error are mainly due to the level of measurement noise of the hot-film sensor signals which perturb the efficiency of the controller. Moreover, while the PI controller is found to achieve satisfactorily a given output target, the characteristic time for reattachment ($\tau_r = 28.1Hs/U_\infty$) is however not found to be significantly reduced compared to the open-loop configuration with continuous blowing.

5.2. Set point tracking

To reduce the actuation cost and the variations in DC which were found significant for a PI controller, optimal set point tracking is now examined. Note that a constant step reference input is considered while the tracking problem has been solved for more general classes of reference inputs. State feedback (or linear quadratic tracking, LQT) and observer-based output feedback (extension of linear quadratic gaussian regulator to tracking problem) control designs based on the linear models established in section 4 are considered.

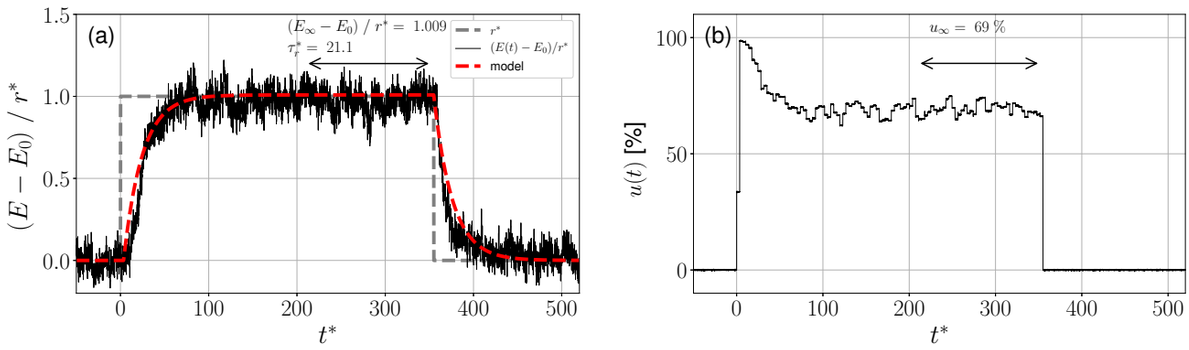

Figure 10: Results for LQR controller for $Q = 10000$, $R = 1$, $K = 46.8$ and $K_r = 130.2$. (a) friction gain $E(t) - E_0$ and corresponding steady value $E_\infty - E_0$ and characteristic time τ_r^*, (b) duty cycle $DC(t)$ and corresponding steady value DC_∞.

5.2.1. Linear quadratic tracking

Let consider the initial plant described by Eq. (2) and here rewritten, in conventional form, as,

$$\left\{ \begin{array}{rcl} \dot{x}(t) & = & A \quad x(t) \quad + \quad B \quad u(t - t_d) \\ y(t) & = & C \quad x(t) \end{array} \right. \tag{9}$$

i.e with $A = -(1/\tau_r)$, $B = (E_\infty - E_0)/\tau_r$ and $C = 1$. The goal of the optimal tracking problem is to find the optimal control law $\tilde{u}$ such that the system tracks asymptotically the reference trajectory in an optimal manner. The theoretical developments of the LQT are given in Appendix A. In the present case, the state, observation and control variables in Eq. (9) are one-dimensional. In addition, since $C = 1$, the state variable is assumed to be perfectly known and given by the observation variable. The solution of the LQT problem can be thus simplified. The following quadratic cost functional $\mathcal{J}(x, u)$ defined in finite-time horizon is considered,

$$\mathcal{J}(x, u) = \frac{1}{2} r^{*2} + \int_{t_0}^{t_f} \left[\ Q(x(t) - r^*)^2 \quad + \quad Ru(t)^2 \ \right] \ dt \tag{10}$$

The composition of $\mathcal{J}$ is motivated by the need to reduce the error between the desired reference r^* and measured outputs, while having some flexibility with respect to control effort. Note that Q and R reduces here to positive weighting scalars. The standard solution of the linear quadratic tracking (LQT) problem is given by Alba-Florest and Barbierit [61] which in the present case of a one-dimensional problem reduces to,

$$\tilde{u}(t) = -R^{-1} B S \ x(t) + R^{-1} B \ v \tag{11}$$

where S and v are solutions of an algebraic Riccati equation and output differential equation respectively as detailed in Appendix A. The first term in Eq. (11) is the feedback control part that depends on the system state while the second term represents the feedforward control part that depends on the reference trajectory.

The influence of coefficients Q and R on the reactivity and efficiency of the controller can be found in Raibaudo [46]. The main result is that increasing Q leads to an increase of fluctuating values of the DC around its mean while the characteristic time response is poorly affected. Results reported in figure 10 are presented for $Q = 10^4$ and $R = 1$ which gives a similar ratio than that observed for $||u||_2^2/||y||_2^2 \sim 100$. To allow comparisons with the PI controller, the reference value corresponding to 80% of the achievable friction gain obtained in open-loop control with continuous blowing is again considered. Compared to the previous results obtained with the PI controller, the state error is reduced ($e_\infty/r^* < 1\%$). As observed in figure 10(b), the variance of the control command is also significantly reduced in the steady regime. In contrast, the characteristic rising time τ_r and the DC_∞ achieved for the steady state are comparable to that obtained with the PI controller. Note that other reference values have been tested and similar observations have been made (see [46] for details). At this stage, the LQT tracking controller is found to fulfill the theoretical objectives but without outperforming significantly the PI controller.

5.2.2. Control with tracking using linear-quadratic-gaussian regulator

In the previous section, a linear-quadratic regulator was implemented by considering that the flow state could be fully represented by a single hot-film sensor. As mentioned in §4.3, hot-film sensor signals are generally contaminated by noise and these perturbations should therefore be taken into account when designing the controller. A Kalman filter was used in Eq. (6) to obtain a model estimate of the separation length $x^L(t)$, based on the measurement

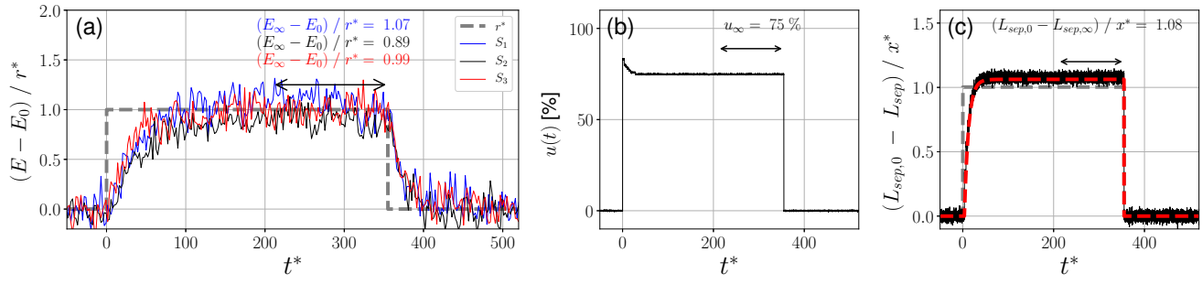

Figure 11: Results for LQG controller using three hot-film sensors. (a) Friction gain $E(t) - E_0$ and corresponding steady value $E_\infty - E_0$ for each sensor, scaled by the target r^*, (b) duty cycle $DC(t)$ and corresponding steady value DC_∞, (c) estimation of the separation length reduction $L_{sep,0} - L_{sep}$, scaled by the equivalent target $x^* = 0.24$ m.

of the friction gain to take into account for measurement noise. Combining this estimator to a linear-quadratic regulator leads into a linear-quadratic-gaussian (LQG) problem. The observed-based output feedback controller that solves this new problem and which minimises the cost functional $\mathcal{J}$ defined in §5.2.1, can be read as, using conventional notations [62],

$$\left\{ \begin{array}{rcrcrcl} \dot{\widehat{x}}^L(t) & = & \widehat{A} & \widehat{x}^L(t) & + & \widehat{B}\tilde{u}(t) & + \quad \mathbb{L}(\mathbf{y}(t) - \widehat{C}\widehat{x}^L(t)) \\ \tilde{u}(t) & = & -\widehat{K} & \widehat{x}^L(t) & + & \widehat{K}_r r^* & \end{array} \right. \tag{12}$$

with $\widehat{A}$, $\widehat{B}$ and $\mathbb{L}$ scalars defined in Eq. (6). Terms $\widehat{K}$ and $\widehat{K}_r$ denotes the controller and tracking gains respectively.

Results for the LQG controller are presented in figure 11. The optimal command law is shown in figure 11(b), while responses to this actuation of the friction gain measured by the three hot-film sensors are reported in figure 11(a), and the response of the estimated separation length reduction in figure 11(c). The static error is found to be different for the three hot-film signals $\{s_1, s_2, s_3\}$, being respectively $e_1 = +7\%$, $e_2 = -11\%$ and $e_3 = -1\%$. This can be explained by differences of dynamics between each sensor and also the separation length. However, the mean steady error $\overline{e} = (|e_1| + |e_2| + |e_3|) \,/\, 3 = 6\%$ is comparable with the LQR response. Compared to the previous controllers, the overshoot of DC at the actuation opening is reduced by 20 %. The DC then stabilizes rapidly to a steady value of 75 % higher than previous controllers command but with negligible variations.

Given $r^* = 0.8V$, the targetted value for the separation length reduction becomes $\widehat{x^*}/H_s = 1.37$. A steady error of $+8\%$ is observed on the steady separation length reduction and corresponds approximately to the previous error observed on the friction gain. In conclusion, the LQG controller is found to overperform the previous controllers in terms of stability and to be less sensitive to the sensors noise.

5.3. Robust control

Previous controllers succeed to reach fixed set of performances (precision, cost optimality, noise influence reduction, etc.). These performances have to be guaranteed despite changes of operating conditions or again incoming perturbations at least in a given acceptable range. In such situation, robust control should be examined. A $\mathcal{H}_\infty$ control is here considered by following the procedure initially suggested by Boyd and Barratt [63]. In the following, the first-order model for the friction gain established in §6 is first revisited by accounting for exogenous inputs acting as disturbances on the system (§5.3.1). The main elements of the $\mathcal{H}_\infty$ control is then explained in §5.3.2. Finally, results of the $\mathcal{H}_\infty$ control for the present study are presented and discussed in §5.3.3.

5.3.1. 1-DOF controlled plant

The one-degree-of-freedom (1-DOF) control system presented in figure 12 is considered. The goal in the design of 1-DOF control system is to keep the system output y_p close to the reference signal r^* despite the disturbances n_{proc}, the actuator-referred process noise, and n_{sensor}, the sensor noise, while ensuring that the actuator signal u is not too large [63]. The particularity of such regulator is that the controller processes only the tracking error signal corrupted by the sensor noise, hereafter $y = r^* - (y_p + n_{sensor})$, to produce the actuator signal u. The reference signal along with the process and sensor noises are exogenous inputs, while the control signal and the system output are both outputs of the controlled system, leading to defined the following input and output vectors,

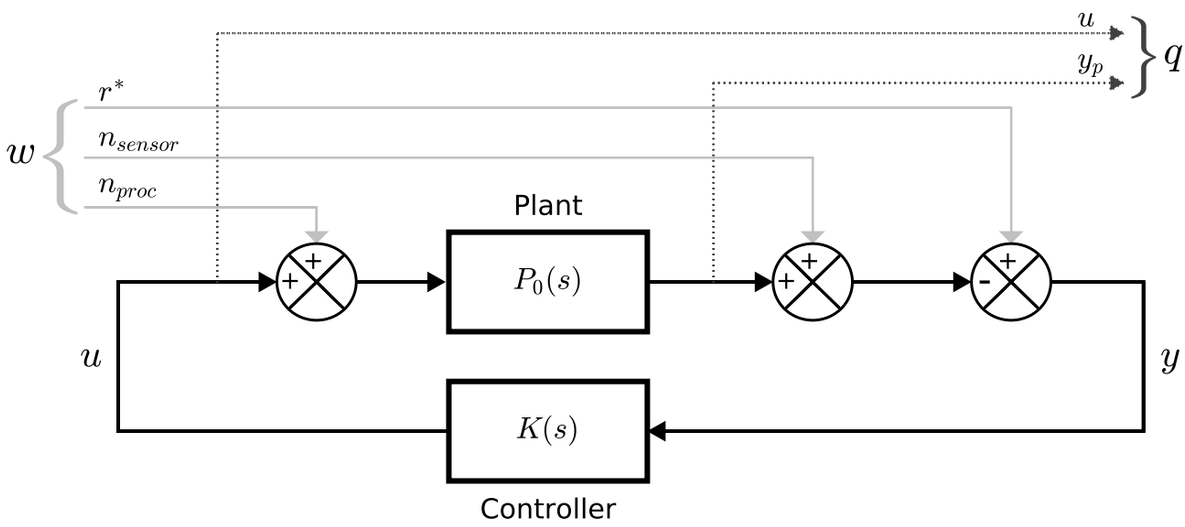

Figure 12: One degree of freedom (1-DOF) model form from the controlled plant (inspired from Boyd and Barratt [63]).

w and q respectively,

$$w = \begin{bmatrix} n_{proc} \\ n_{sensor} \\ r^* \end{bmatrix} \quad q = \begin{bmatrix} y_p \\ u \end{bmatrix} \tag{13}$$

such that the state-space representation of the plant considered can be expressed as,

$$\begin{bmatrix} q \\ \hline y \end{bmatrix} = P(s) \begin{bmatrix} w \\ \hline u \end{bmatrix} \tag{14}$$

with $P(s)$ the input-output transfer matrix given by,

$$P(s) = \left[\begin{array}{c|c} P_{qw}(s) & P_{qu}(s) \\ \hline P_{yw}(s) & P_{yu}(s) \end{array}\right] = \left[\begin{array}{ccc|c} P_0(s) & 0 & 0 & P_0(s) \\ 0 & 0 & 0 & 1 \\ \hline -P_0(s) & -1 & 1 & -P_0(s) \end{array}\right] \tag{15}$$

with $P_0(s)$ the state-space representation of the dynamics expressed with Laplace transform.

5.3.2. Definition and resolution of $\mathcal{H}_\infty$ problem

Considering a transfer function matrix $H(s)$ defined from a linear time-invariant system, the $\mathcal{H}_\infty$ norm is defined for stable systems space by:

$$||H(s)||_\infty = \sup_{\omega \in \mathbb{R}} \{ \max_{\lambda_i}(H(j\omega)) \} \tag{16}$$

From the transfer function $P(s)$ (Eq. 15), the global transfer function between the input $Q(s) = \mathcal{L}\{q\}$ and the output $W(s) = \mathcal{L}\{w\}$, with $\mathcal{L}$ the Laplace transform, is expressed using a Linear Fractional Transformation $\mathcal{M}_{P,K}$:

$$\begin{cases} Q(s) &= \mathcal{M}_{P,K}\ W(s) \\ \mathcal{M}_{P,K} &= P_{qw}(s) + P_{qu}(s)K(s)(I - P_{yu}(s)K(s))^{-1}P_{yw}(s) \end{cases} \tag{17}$$

with $K(s)$ the controller function. The $\mathcal{H}_\infty$ standard problem is, for $P(s)$ and $\gamma > 0$ fixed, to find the transfer function $K(s)$ stabilizing the system (Fig. 12) and verifying the condition: $||\mathcal{M}_{P,K}||_\infty < \gamma$. The $\mathcal{H}_\infty$ optimal problem is to find controllers verifying the $\mathcal{H}_\infty$ standard problem with minimal values of γ. The $\mathcal{H}_\infty$ standard problem is resolved here using the Ricatti equations (also named Glover-Doyle technique [64]). At the end, a state-representation of the controller is obtained fulfilling the $\mathcal{H}_\infty$ problem and is implemented directly for our experiments.

5.3.3. Results for the present work

For the present study, a first-order model has been established for the dynamics (eq. 2). It corresponds to a first-order transfer function $P_0(s) = K\ /\ (1 + \tau_r s)$ *expressed in Laplace transform* . The procedure described

previously to obtain a $\mathcal{H}_\infty$ control (§5.3.2) provides a state-space representation of this controller expressed as:

$$\left\{ \begin{array}{rcccc} \dot{x_c}(t) & = & (-1/\tau_c) & x_c(t) & + & \alpha_{xy,c} & y_p(t) \\ u(t) & = & \alpha_{ux,c} & x_c(t) & & & \end{array} \right. \tag{18}$$

with $\tau_c = 0.98$ s the controller characteristic time, $\alpha_{xy,c} = -2.5 \times 10^{-3}\ s^{-1}$ and $\alpha_{ux,c} = -1.1 \times 10^{-3}\ (V.s)^{-1}$ gains. Results of this $\mathcal{H}_\infty$ controller for our present case are presented in figure 13. In comparison with the previous closed-loop controllers, the $\mathcal{H}_\infty$ control reaches similar efficiency in terms of precision and dynamics. The characteristic time is $\tau_r^* = 15.5$. This time is lower than the ones found from previous controllers. However, the hot-film signal needs time to stabilize and shows overshoots and oscillations around the steady regime. The controller dynamics $\tau_c^* = 69$ is higher than the characteristic time from the open-loop characterization. The controller reacts more slowly for the stabilization of quick fluctuations. The temporal evolution of the duty cycle (Fig. 13 (b)) is smoother compared to the other controllers. The steady duty cycle $DC_\infty = 70\%$ is equivalent to the one found for example for the optimal LQR control.

The objective in this section is to observe the dynamical response of the flow under $\mathcal{H}_\infty$ control under a sudden perturbation of the incoming boundary layer. The robustness of $\mathcal{H}_\infty$ control is here qualitatively estimated by comparison with an other non-robust controller such as PI controller. A disturber is put at $\Delta X_{dist}\ /\ H_s = 4.5$ upstream the separation line to perturb the incoming boundary layer. It consists in a cambered plate of $0.24H_s$ long (X direction), $0.011H_s$ high (Y direction) and covers the all wind-tunnel span. The disturber is fixed at its extremities by two cylinders, which set the rotation axis parallel to the span direction and allows the movement to be driven outside the wind-tunnel. During the rotation, the disturber remains mostly planar and the perturbation is considered two-dimensional. The angle between the disturber surface and the flat plate is noted θ_{dist}. The perturbation procedure is as follows: the closed-loop controller considered is first activated during a period long enough to reach the steady regime. Quick perturbations are then realized: every ten seconds (equivalent to

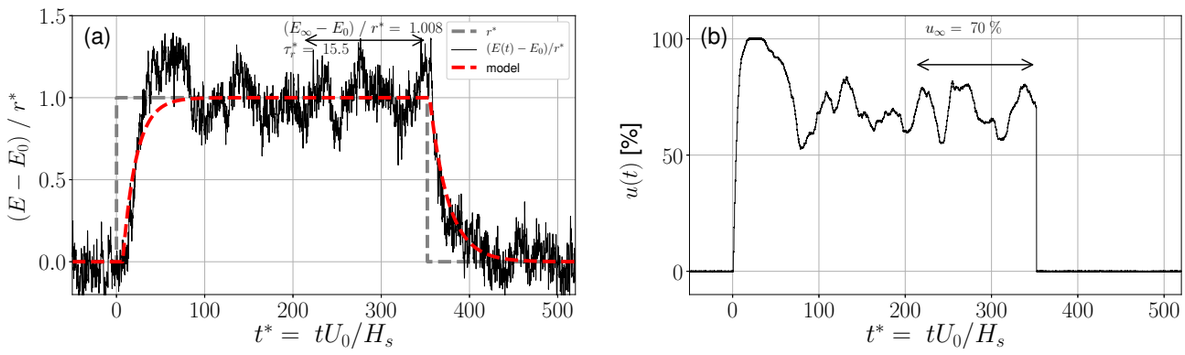

Figure 13: Results for $\mathcal{H}_\infty$ controller. (a) friction gain $E(t) - E_0$ and corresponding steady value $E_\infty - E_0$ and characteristic time τ_r^*, (b) duty cycle $DC(t)$ and corresponding steady value DC_∞.

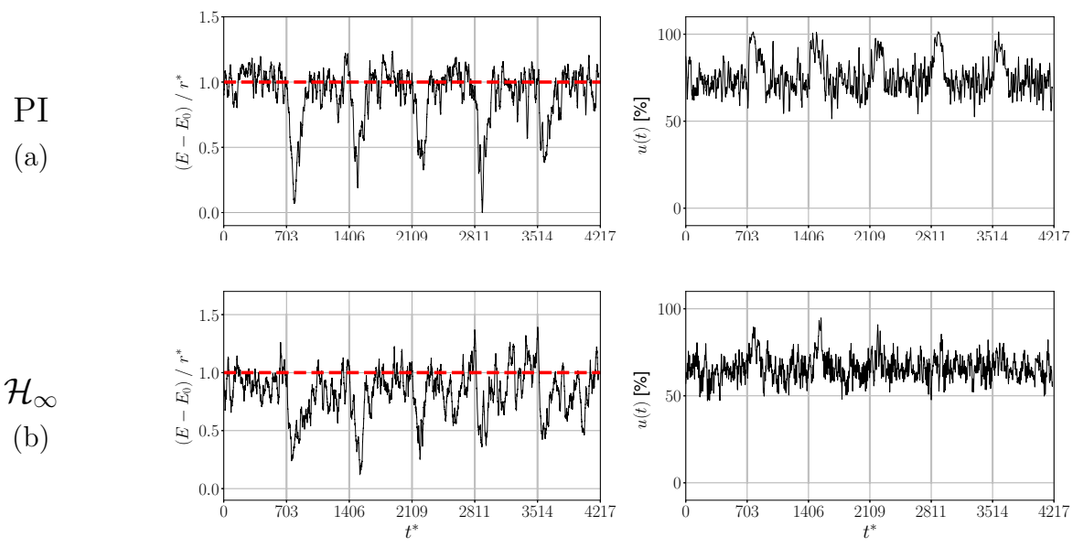

Figure 14: Test of robustness for (a) PI controller and (b) $\mathcal{H}_\infty$ controller. Every ten seconds (equivalent to $t^* \sim 703$), the disturber is activated manually for approximately two seconds ($t^* \sim 141$)

$t^* \sim 703$), the disturber, initially flattened to the wall ($\theta_{dist} = 0°$), is lifted at a maximum angle of $\theta_{dist} \sim 50°$ for 1 second approximatively, and comes down for the same period. *This maximal angle corresponds to a penetration of the boundary layer height δ_0 of about 17 %, so almost half of the penetration achieved by the actuators jets.* The synchronization between the acquisition and the perturbation was not possible automatically. Consequently, three packages of 60 seconds are acquired and averaged together. The results of this procedure are presented in figure 14 for two closed-loop controllers: (a) PI control (theoretically not considered as a robust controller) and (b) $\mathcal{H}_\infty$ robust control. For each subfigure, gray lines indicate the disturber activation instants (every 10 s or $t^* \sim 703$) and red line corresponds to the target scaled. For PI control, high perturbations are observed for the friction signal and the duty cycle. The command almost reaches the continuous actuation after each perturbation. The controller is not able to limit these perturbations without sudden changes of its command. On the contrary, friction signal perturbations are significantly reduced in amplitude using $\mathcal{H}_\infty$ controller in figure (b). The duty cycle observed reacts more smoothly to external perturbations. Peaks of duty cycle are reduced by almost a half. Consequently, $\mathcal{H}_\infty$ control provides additional robustness to the feedback control and is found to be able to resist to strong perturbations of the initial conditions.

Conclusions

Experimental closed-loop control of a ~~massively~~ separated boundary layer in high Reynolds number regime was presented. While the main objective of the paper is to apply robust control (with regards to changes in the incoming flow) comparisons between different model-based closed-loop controllers were also discussed. The actuators consisted in pulsed round air jets located few steps upstream where the boundary layer occurs separation due to the presence of an inclined flap.

Different models for the plant (here including the flow itself, the actuation and sensors set-up) have been considered for closed-loop control to achieve increasing efficiency in terms of reactivity, control cost and robustness. The phase-averaged response to actuation of hot-film sensors located in the separation region was first considered as a local representation of the overall flow response. The transient response of these sensors was found to be well modelled by to a first-order model with delay with appropriate characteristic reattachment/separation times. The phase-averaged response of the recirculation length was then studied as it constitutes a more appropriate quantity to represent instantaneously the global flow state in the separated region. Thanks to phase-locked PIV measurements, the transient response of the recirculation length to continuous actuation was found, again, to be well represented by a first-order model. The time delay $t_d^* = t_d U_0/H_s$ and characteristic reattachment time $\tau^* = \tau U_0/H_s$ were estimated respectively as 3.9 and 21.1 for the friction gain, 3.5 and 9.1 for the separation length. Since the recirculation length was however not accessible in real-time, its use in a control application is difficult to implement. To overcome this difficulty, a steady-state Kalman filter was employed to obtain a real-time estimator of the separation length from hot-film signals and actuation command values.

Considering these different models, feedback controllers have been then designed and implemented experimentally. A summary of the performances achieved by the different controllers examined in terms of static error, reactivity and duty-cycle achieved in the steady regime is reported in Tab. 2. Proportional-Integral (PI) controller, generally considered as a reference control, was implemented to reduce the error $e(t)$ between a target value r^* chosen arbitrarily and the friction gain signal. A linear quadratic regulator was then considered and was found to reduce both the static error and characteristic time for similar values of steady actuation DC_∞. In addition to cost consideration, a linear quadratic gaussian regulator allowing to deal with noisy plant outputs was tested and found to achieve similar performances of control. In the end, a robust $\mathcal{H}_\infty$ controller was implemented and was found to maintain the flow in an attached regime despite large incoming perturbations and sensor noises.

Appendix A: Finite-time continuous Linear Quadratic Tracking control problem

Let consider the following linear-time invariant (LTI) system,

$$\begin{cases} F(\mathbf{x},\mathbf{u}) &= \dot{\mathbf{x}}(t) - A\mathbf{x}(t) + B\mathbf{u}(t) &= 0 \\ y(t) &= C\mathbf{x}(t) \end{cases} \tag{19}$$

Controller	**Error** $\lvert e_\infty \rvert / r^*$	**Dynamics** τ_r^*	**Duty cycle** DC_∞
PI	9 %	28.1	65 %
LQR	1 %	21.1	69 %
LQG	6 %	28.1	75 %
$\mathcal{H}_\infty$	6 %	15.5	70 %

Table 2: Summary of the closed-loop control results.

Assume that we aim at driving the output of the system following a desired reference value $\mathbf{y_c}$ in the finite time interval $[t_0, t_f]$, with a minimal cost of control energy. The optimal tracking problem is defined as the problem of finding an optimal control law $\mathbf{u}^\star$ such that the following quadratic cost function is minimised,

$$\mathcal{J}(\mathbf{x},\mathbf{u}) = \frac{1}{2}\mathbf{x}^\intercal(t_f)C^\intercal C\mathbf{x}(t_f) + \frac{1}{2}\int_{t_0}^{t_f}\left[(\mathbf{y_c} - C\mathbf{x}(t))^\intercal\, Q\,(\mathbf{y_c} - C\mathbf{x}(t)) + \mathbf{u}^\intercal(t)R\mathbf{u}(t)\right] \tag{20}$$

with R a symmetric positive definite matrix, and Q a symmetric non negative definte matrix. We here assume that all the states and outputs are completely measurable.
Let introduce the Lagrangian functional L defined as,

$$\mathcal{L}(\mathbf{x},\mathbf{u},\boldsymbol{\lambda}) = \mathcal{J}(\mathbf{x},\mathbf{u}) - < F(\mathbf{x},\mathbf{u}),\boldsymbol{\lambda} > \tag{21}$$

where $\boldsymbol{\lambda}$ denotes the adjoint variable of the problem. The problem reduces now to an unconstrained optimisation problem where one needs to determine the state variable, the control law and the adjoint variables such that $\mathcal{L}(\mathbf{x},\mathbf{u},\boldsymbol{\lambda})$ reaches an extremum. Assuming variable separation this results in the following three conditions,

$$\nabla_{\mathbf{x}}\mathcal{L} = 0 \quad , \quad \nabla_{\mathbf{u}}\mathcal{L} = 0 \quad , \quad \nabla_{\boldsymbol{\lambda}}\mathcal{L} = 0 \tag{22}$$

where the Frechet derivative is here used. Soling the first condition leads to retrieve the state equation. The second condition leads to the optimal condition, which in the present case reads as,

$$\mathbf{u}^*(t) = -R^{-1}B^\intercal\boldsymbol{\lambda}^*(t) \tag{23}$$

Finally, the third condition leads to the adjoint equation which in the present case reduces to,

$$-\dot{\boldsymbol{\lambda}}(t) = C^\intercal QC\mathbf{x}(t) + A^\intercal\boldsymbol{\lambda}(t) \tag{24}$$

The adjoint variable can be found from the state variable using the linear relationship,

$$\boldsymbol{\lambda}^*(t) = S(t)\mathbf{x}(t) + v(t) \tag{25}$$

This results in the optimal control law,

$$\mathbf{u}^*(t) = -R^{-1}B^\intercal S(t)\mathbf{x}(t) - R^{-1}B^\intercal v(t) \tag{26}$$

where $S(t)$, a symmetric definite positive matrix, and $v(t)$ are respectively the solutions of the equations,

$$\begin{aligned} -\dot{S}(t) &= S(t)A + A^\intercal S(t) - S(t)BR^{-1}B^\intercal S(t) + C^\intercal QC \\ -\dot{v}(t) &= -\left(A^\intercal - S(t)BR^{-1}B^\intercal\right)v(t) + C^\intercal Q y_c(t) \end{aligned} \tag{27}$$

satisfying the boundary conditions,

$$\begin{aligned} S(t_f) &= C^\intercal C \\ m(t_f) &= -C^\intercal y_c(t_f) \end{aligned} \tag{28}$$

Acknowledgments

The present work is supported by the Agence National de la Recherche (ANR) through the french ANR project SePaCode (ANR-11-BS09-0018) and by the CISIT International Campus through the Contraéro project. The authors are indebted J.P. Richard, A. Polyakov and D. Efimov (INRIA-CRIStAL) for technical discussions about closed-loop control, M. Stanislas (LMFL) for scientific discussions about the physics of turbulence control, C. Cuvier (LMFL) for his help during the experiments and for the data processing.

References

[1] M. Gad-el hak, Flow control: passive, active and reactive flow management, cambridge Edition, 2000.

[2] D. W. Bechert, M. Bartenwerfer, The viscous flow on surfaces with longitudinal ribs, Journal of Fluid Mechanics 206 (-1) (1989) 105. doi:10.1017/S0022112089002247.
URL http://www.journals.cambridge.org/abstract{_}S0022112089002247

[3] H. D. Taylor, The elimination of diffuser separation by vortex generators, Tech. rep., United Aircraft Corporation, East Hartford, Connecticut (1947).

[4] J. C. Lin, F. G. Howard, G. V. Selby, Turbulent flow separation control through passive techniques, in: 2nd Shear Flow Conference, American Institute of Aeronautics and Astronautics, Tempe, USA, 1989. doi:10.2514/6.1989-976.
URL http://arc.aiaa.org/doi/pdf/10.2514/6.1989-976http://arc.aiaa.org/doi/abs/10.2514/6.1989-976

[5] K. P. Angele, B. Muhammad-Klingmann, The effect of streamwise vortices on the turbulence structure of a separating boundary layer, European Journal of Mechanics, B/Fluids 24 (5) (2005) 539–554. doi:10.1016/j.euromechflu.2005.01.005.
URL http://linkinghub.elsevier.com/retrieve/pii/S0997754605000270

[6] G. Godard, M. Stanislas, Control of a decelerating boundary layer. Part 1: Optimization of passive vortex generators, Aerospace Science and Technology 10 (3) (2006) 181–191. doi:10.1016/j.ast.2005.11.007.

[7] D. A. Compton, J. P. Johnston, Streamwise vortex production by pitched and skewed jets in a turbulent boundary layer, AIAA Journal 30 (3) (1992) 640–647. doi:10.2514/3.10967.

[8] C. Tilmann, K. Langan, J. Betterton, M. Wilson, Characterisation of pulsed vortex generator jets for active flow control, Symposium on "Active Control Technology" for Enhanced Performance Operational Capabilities of Military Aircraft, Land Vehicles and Sea Vehicles.

[9] G. V. Selby, J. C. Lin, F. G. Howard, Control of low-speed turbulent separated flow using jet vortex generators, Experiments in Fluids 12 (6) (1992) 394–400. doi:10.1007/BF00193886.

[10] G. Godard, M. Stanislas, Control of a decelerating boundary layer. Part 3: Optimization of round jets vortex generators, Aerospace Science and Technology 10 (6) (2006) 455–464. doi:10.1016/j.ast.2005.11.005.

[11] C. Cuvier, Active control of a separated turbulent boundary layer in adverse pressure gradient, Ph.D. thesis, École Centrale de Lille (2012).

[12] P. Cathalifaud, G. Godard, C. Braud, M. Stanislas, The flow structure behind vortex generators embedded in a decelerating turbulent boundary layer, Journal of Turbulence 10 (42) (2009) 1–37. doi:10.1080/14685240903273881.
URL http://www.tandfonline.com/doi/abs/10.1080/14685240903273881

[13] S. Gopalan, B. M. Abraham, J. Katz, The structure of a jet in cross flow at low velocity ratios, Physics of Fluids 16 (6) (2004) 2067–2087. doi:10.1063/1.1697397.

[14] J. Kostas, J.-M. Foucaut, M. Stanislas, The flow structure produced by pulsed-jet vortex generators in a turbulent boundary layer in an adverse pressure gradient, Flow, Turbulence and Combustion 78 (2007) 331–363. doi:10.1007/s10494-007-9069-3.

[15] O. Lögdberg, J. H. M. Fransson, P. H. Alfredsson, Streamwise evolution of longitudinal vortices in a turbulent boundary layer, Journal of Fluid Mechanics 623 (2009) 27. doi:10.1017/S0022112008004825.
URL http://www.journals.cambridge.org/abstract{_}S0022112008004825

[16] D. Greenblatt, I. J. Wygnanski, Control of flow separation by periodic excitation, Progress in Aerospace Sciences 36 (7) (2000) 487–545. doi:10.1016/S0376-0421(00)00008-7.
URL http://linkinghub.elsevier.com/retrieve/pii/S0376042100000087

[17] K. McManus, H. Legner, S. Davis, Pulsed vortex generator jets for active control of flow separation, in: AIAA paper, American Institute of Aeronautics and Astronautics, Colorado Springs, USA, 1994. doi:10.2514/6.1994-2218.

[18] J. Ortmanns, M. Bitter, C. J. Kähler, Dynamic vortex structures for flow-control applications, Experiments in Fluids 44 (3) (2008) 397–408. doi:10.1007/s00348-007-0442-8.

[19] S. G. Siegel, J. Seidel, C. Fagley, D. M. Luchtenburg, K. Cohen, T. Mclaughlin, Low-dimensional modelling of a transient cylinder wake using double proper orthogonal decomposition, Journal of Fluid Mechanics 610 (2008) 1–42. doi:10.1017/S0022112008002115.
URL http://www.journals.cambridge.org/abstract{_}S0022112008002115

[20] R. Mathis, A. Lebedev, E. Collin, J. Delville, J. P. Bonnet, Experimental study of transient forced turbulent separation and reattachment on a bevelled trailing edge, Experiments in Fluids 46 (1) (2009) 131–146. doi:10.1007/s00348-008-0549-6.

[21] A. Darabi, I. Wygnanski, Active management of naturally separated flow over a solid surface. Part 1. The forced reattachment process, Journal of Fluid Mechanics 510 (2004) 105–129. doi:10.1017/S0022112004009231.

[22] M. Amitay, A. Glezer, Controlled transients of flow reattachment over stalled airfoils, International Journal of Heat and Fluid Flow 23 (5) (2002) 690–699. doi:10.1016/S0142-727X(02)00165-0.

[23] G. T. K. Woo, T. Crittenden, A. Glezer, Transitory separation control over a stalled airfoil, in: 39th AIAA Fluid Dynamics Conference, American Institute of Aeronautics and Astronautics, San Antonio, USA, 2009. doi:10.2514/6.2009-4281.

[24] W. L. Siauw, J. P. Bonnet, J. Tensi, L. Cordier, B. R. Noack, L. Cattafesta, Transient dynamics of the flow around a NACA 0015 airfoil using fluidic vortex generators, International Journal of Heat and Fluid Flow 31 (3) (2010) 450–459. doi:10.1016/j.ijheatfluidflow.2010.02.028.

[25] T. Shaqarin, C. Braud, S. Coudert, M. Stanislas, Open and closed-loop experiments to identify the separated flow dynamics of a thick turbulent boundary layer, Experiments in Fluids 54 (2) (2013) 1448. doi:10.1007/s00348-012-1448-4.

[26] C. Raibaudo, M. Stanislas, F. Kerhervé, Transient Characterization of the Reattachment of a Massively Separated Turbulent Boundary Layer Under Flow Control, Flow, Turbulence and Combustion 98 (4) (2017) 1039–1063. doi:10.1007/s10494-016-9796-4.

[27] B. G. Allan, J.-N. Juang, D. L. Raney, A. Seifert, L. G. Pack, D. E. Brown, Closed-loop Separation Control Using Oscillatory Flow Excitation, Tech. rep., NASA (2000).

[28] R. Becker, M. Garwon, C. Gutknecht, G. Bärwolff, R. King, Robust control of separated shear flows in simulation and experiment, Journal of Process Control 15 (6) (2005) 691–700. doi:10.1016/j.jprocont.2004.12.001.
URL http://www.sciencedirect.com/science/article/pii/S095915240500003Xhttp://linkinghub.elsevier.com/retrieve/pii/S095915240500003X

[29] L. Henning, R. King, Multivariable closed-loop control of the reattachement length downstream of a backward-facing step, in: P. Zítek (Ed.), 16th IFAC World Congress, Praha, Czech Republic, Praha, Czech Republic, 2005, pp. 1999–1999. doi:10.3182/20050703-6-CZ-1902.02000.
URL http://www.nt.ntnu.no/users/skoge/prost/proceedings/ifac2005/Fullpapers/02575.pdf

[30] Y. Tian, L. N. Cattafesta, R. Mittal, Adaptive Control of Separated Flow, in: 44th AIAA Aerospace Sciences Meeting and Exhibit, American Institute of Aeronautics and Astronautics, Reno, Nevada, USA, 2006. doi:10.2514/6.2006-1401.

[31] R. Becker, R. King, R. Petz, W. Nitsehe, Adaptive Closed-Loop Separation Control on a High-Lift Configuration using Extremum Seeking, AIAA Journal 45 (6) (2007) 1382–1392.

[32] M. Pastoor, L. Henning, B. R. Noack, R. King, G. Tadmor, Feedback shear layer control for bluff body drag reduction, Journal of Fluid Mechanics 608 (2008) 161–196. doi:10.1017/S0022112008002073.
URL http://www.journals.cambridge.org/abstract{_}S0022112008002073

[33] N. Benard, E. Moreau, J. Griffin, L. N. Cattafesta, Slope seeking for autonomous lift improvement by plasma surface discharge, Experiments in Fluids 48 (5) (2010) 791–808. doi:10.1007/s00348-009-0767-6.

[34] J. Poggie, C. Tilmann, P. Flick, J. Silkey, B. Osborne, G. Ervin, D. Maric, S. Mangalam, A. Mangalam, Closed-Loop Stall Control on a Morphing Airfoil Using Hot-Film Sensors and DBD Actuators, in: 48th AIAA Aerospace Sciences Meeting Including the New Horizons Forum and Aerospace Exposition, American Institute of Aeronautics and Astronautics, Orlando, USA, 2010. doi:10.2514/6.2010-547.
URL http://arc.aiaa.org/doi/abs/10.2514/6.2010-547

[35] N. O. Packard, Active Flow Separation Control of a Laminar Airfoil at Low Reynolds Number, Ph.D. thesis, Ohio State University (2012).
URL https://etd.ohiolink.edu/!etd.send{_}file?accession=osu1338315982{&}disposition=inline

[36] N. Gautier, J.-L. Aider, Control of the detached flow behind a backward-facing step by visual feedback, arXiv preprint arXiv:1306.4554 469 (2013) 1–15. arXiv:arXiv:1306.4554v1, doi:10.1098/rspa.2013.0404.
URL http://arxiv.org/abs/1306.4554http://rspa.royalsocietypublishing.org/cgi/doi/10.1098/rspa.2013.0404

[37] T. Duriez, V. Parezanovic, K. Von˜Krbek, L. Cordier, B. R. Noack, J.-P. Bonnet, M. Segond, M. W. Abel, N. Gautier, J.-L. Aider, C. Raibaudo, C. Cuvier, M. Stanislas, A. Debien, N. Mazellier, A. Kourta, S. L. Brunton, Closed-loop control of experimental shear flows using MLC, 67th Annual Meeting of the APS Division of Fluid Dynamics 59 (20).
URL http://meetings.aps.org/Meeting/DFD14/Session/R12.7

[38] S. Shimomura, S. Sekimoto, A. Oyama, K. Fujii, H. Nishida, Closed-Loop Flow Separation Control Using the Deep Q Network over Airfoil, AIAA Journal (2020) 1–11doi:10.2514/1.j059447.

[39] S. Obeid, G. Ahmadi, R. Jha, NARMAX Identification Based Closed-Loop Control of Flow Separation over NACA 0015 Airfoil, Fluids 5 (3) (2020) 100. doi:10.3390/fluids5030100.
URL https://www.mdpi.com/2311-5521/5/3/100

[40] M. Bergmann, L. Cordier, Optimal control of the cylinder wake in the laminar regime by trust-region methods and POD reduced-order models, Journal of Computational Physics 227 (16) (2008) 7813–7840. doi:10.1016/j.jcp.2008.04.034.
URL http://www.sciencedirect.com/science/article/pii/S0021999108002659http://linkinghub.elsevier.com/retrieve/pii/S0021999108002659

[41] C. W. Rowley, V. Juttijudata, D. R. Williams, Cavity Flow Control Experiments and Simulations, in: 43rd AIAA Aerospace Sciences Meeting and Exhibit, American Institute of Aeronautics and Astronautics, Reno, Nevada, USA, 2005. doi:10.1088/1742-6596/548/1/012068.
URL http://stacks.iop.org/1742-6596/548/i=1/a=012068?key=crossref.66c71fb7e2fe7126bc7d49c4a1c22905

[42] S. J. Illingworth, A. S. Morgans, C. W. Rowley, Feedback control of cavity flow oscillations using simple linear models, Journal of Fluid Mechanics 709 (2012) 223–248. doi:10.1017/jfm.2012.330.
URL http://journals.cambridge.org/abstract{_}S0022112012003308http://www.journals.cambridge.org/abstract{_}S0022112012003308

[43] P.-Y. Pamart, J. Dandois, E. Garnier, P. Sagaut, NARX Modeling and Adaptive Closed-Loop Control of a Separation by Synthetic Jet in Unsteady RANS computations, in: 5th Flow Control Conference, no. July, American Institute of Aeronautics and Astronautics, Chicago, USA, 2010, pp. 1–15. doi:10.2514/6.2010-4971.
URL http://arc.aiaa.org/doi/abs/10.2514/6.2010-4971

[44] J. Carlier, M. Stanislas, Experimental study of eddy structures in a turbulent boundary layer using particle image velocimetry, Journal of Fluid Mechanics 535 (2005) 143–188. doi:10.1017/S0022112005004751.

[45] C. Braud, A. Dyment, Model of an impulsive subsonic jet actuator for flow control applications, Physics of Fluids 24 (4). doi:10.1063/1.3701377.

[46] C. Raibaudo, Characterization of the transient of a separated turbulent boundary layer under control and applications to advanced closed-loop controllers, Ph.D. thesis, École Centrale de Lille (2015).

[47] J.-M. Foucaut, S. Coudert, C. Braud, C. Velte, Influence of light sheet separation on SPIV measurement in a large field spanwise plane, Measurement Science and Technology 25. doi:10.1088/0957-0233/25/3/035304.

[48] A. Seifert, L. P. Melton, Control and identification of turbulent boundary layer separation, in: IUTAM Symposium on One Hundred Years of Boundary Layer Research, Springer, 2006, pp. 199–208.

[49] J. Poggie, C. P. Tilmann, P. M. Flick, J. S. Silkey, B. A. Osbourne, G. Ervin, D. Maric, S. Mangalam, A. Mangalam, Closed-loop stall control system, Journal of Aircraft 47 (5) (2010) 1747–1755.

[50] R. Mathis, A. Lebedev, E. Collin, J. Delville, J.-P. Bonnet, Experimental study of transient forced turbulent separation and reattachment on a bevelled trailing edge, Experiments in Fluids 46 (1) (2009) 131–146.

[51] T. Chabert, J. Dandois, E. Garnier, L. Jacquin, Experimental detection of a periodically forced turbulent boundary layer separation, Experiments in fluids 54 (2) (2013) 1–14.

[52] R. L. Simpson, Turbulent boundary layer separation, Annual Review of Fluid Mechanics 21 (1989) 205–234. doi:10.1016/0376-0421(95)00012-7.

[53] Y. Zhou, Z. J. Wang, Effects of surface roughness on separated and transitional flows over a wing, AIAA Journal 50 (3) (2012) 593–609. doi:10.2514/1.J051237.

[54] R. Becker, M. Garwon, R. King, Development of model-based sensors and their use for closed-loop control of separated shear flows, European Control Conference, ECC 2003 (2003) 3237–3242doi:10.23919/ecc.2003.7086538.

[55] M. Chevalier, J. Hœpffner, E. Åkervik, D. S. Henningson, Linear feedback control and estimation applied to instabilities in spatially developing boundary layers, Journal of Fluid Mechanics 588 (2007) 163–187. doi:10.1017/S0022112007007392.
URL http://www.journals.cambridge.org/abstract{_}S0022112007007392

[56] D. Alazard, Régulation LQ/LQG - Notes de cours, in: ISAE-SUPAERO Courses, 2005.

[57] R. F. Osborn, S. Kota, J. a. Hetrick, D. E. Geister, C. P. Tilmann, J. Joo, Active Flow Control Using High-Frequency Compliant Structures, Journal of Aircraft 41 (3) (2004) 603–609. doi:10.2514/1.111.
URL http://arc.aiaa.org/doi/abs/10.2514/1.111

[58] C. J. Kähler, P. Scholz, J. Ortmanns, R. Radespiel, Towards active control of leading edge stall by means of pneumatic actuators, in: R. King (Ed.), Active Flow Control, Springer Berlin Heidelberg, 2007, Ch. III, pp. 152–172. doi:10.1007/978-3-540-71439-2_10.
URL http://link.springer.com/chapter/10.1007/978-3-540-71439-2{_}10

[59] J.-P. Laval, C. Braud, G. Fournier, M. Stanislas, Large-eddy simulations of control of a separated flow over a 2D bump by means of pulsed jets, Journal of Turbulence 11 (52) (2010) N52. doi:10.1080/14685248.2010.522579.
URL http://www.tandfonline.com/doi/abs/10.1080/14685248.2010.522579

[60] P. Borne, G. Dauphin-Tanguy, J. Richard, F. Rotella, I. Zambettakis, Analyse et régulation des processus industriels, Technip, 1993.

[61] R. Alba-Florest, E. Barbierit, Real-time Infinite Horizon Linear-Quadratic Tracking Controller for Vibration Quenching in Flexible Beams, in: 2006 IEEE International Conference on Systems, Man, and Cybernetics, Taipei, Taiwan, 2020, pp. 38–43. doi:10.1109/ICSMC.2006.384355.

[62] C. Bruni, A. D. Santis, D. Iacoviello, On-line discontinuities identification in noisy signals: Application to Kalman filtering, International Journal of Control 74 (5) (2001) 524–536. doi:10.1080/00207170010018779.

[63] S. Boyd, C. Barratt, Linear controller design: Limits of Performance, Vol. 78, 1991. doi:10.1109/5.52229.

[64] K. Glover, J. C. Doyle, State-space formulae for all stabilizing controllers that satisfy an Hinfinity-norm bound and relations to relations to risk sensitivity, Systems & Control Letters 11 (3) (1988) 167–172. doi:10.1016/0167-6911(88)90055-2.
URL http://www.sciencedirect.com/science/article/pii/0167691188900552